Rapid Communications | Editors' Suggestion

Probing the Berry curvature and Fermi arcs of a Weyl circuit

Yuehui Lu,[1] Ningyuan Jia,[1] Lin Su,[1] Clai Owens,[1] Gediminas Juzeliūnas,[2] David I. Schuster,[1] and Jonathan Simon[1,*]

[1]*The James Franck Institute and Department of Physics, University of Chicago, Chicago, Illinois 60637, USA*

[2]*Institute of Theoretical Physics and Astronomy, Vilnius University, Sauletekio 3, Vilnius LT-10257, Lithuania*

(Received 20 July 2018; published 4 January 2019)

The Weyl particle is the massless fermionic cousin of the photon. While no fundamental Weyl particles have been identified, they arise in condensed matter and metamaterial systems, where their spinor nature imposes topological constraints on low-energy dispersion and surface properties. Here we demonstrate a topological circuit with Weyl dispersion at low momentum, realizing a 3D lattice that behaves as a half-flux Hofstadter model in all principal planes. The circuit platform provides access to the complete complex-valued spin texture of all bulk and surface states, thereby revealing not only the presence of Weyl points and the Fermi arcs that connect their surface projections, but also the Berry curvature distribution through the Brillouin zone and the associated quantized chiral charge of the Weyl points. This work opens a path to exploration of interacting Weyl physics in superconducting circuits, as well as studies of how manifold topology impacts band topology in three dimensions.

DOI: 10.1103/PhysRevB.99.020302

Creating and probing particles with topologically nontrivial dispersion is a growing endeavor with benefits from exploration of exotic emergent phenomenology in many-body physics [1–3] to next-generation technologies (e.g., waveguides [4] and circulators [5]). In two dimensions, successes range from synthetic realizations of graphene [6,7] and Haldane's model [8] to spin-orbit coupling [9,10] and gauge fields [11–20]. Of particular interest are implementations compatible with strong interactions between individual quantized excitations, where extensions to the strongly correlated regime are possible. Candidate platforms include ultracold atoms in optical lattices [21], microwave photons in superconducting circuits [22], and Rydberg-dressed photons [23] in optical resonators [24].

Recently, there has been growing interest in exploring the properties of three-dimensional quasiparticles, with a particular focus on Weyl particles [25], as they have *not* been observed in nature. With a Hamiltonian of the form $H \sim \boldsymbol{\sigma} \cdot \boldsymbol{p}$, these massless particles have a linear dispersion $E \propto \pm|\boldsymbol{p}|$, and are *chiral*, meaning that their eigenstates exhibit momentum-dependent spin texture, with a spin-momentum aligned high-energy branch, and an antialigned low-energy branch: The momentum acts as an effective *Zeeman* field for the spin in a 3D analog of the Dirac fermion [6,7]. The additional symmetries of a lattice system prevent Weyl dispersion over the full Brillouin zone (BZ), restricting the behavior to the vicinity of "Weyl points."

Weyl dispersion has recently been observed in optical, microwave, and phononic metamaterials: A type-I Weyl node, corresponding to a pointlike Fermi surface with linear dispersion, was imaged in the projected dispersion relation of a gyroid microwave material via angle-resolved transmission [26] and the robustness of the surface states demonstrated through introduction of local defects [27]; a type-II Weyl node, a highly tilted Weyl dispersion (see Fig. 5 of Ref. [25]) where particle and hole pockets touch at a point [28,29], was observed through conical diffraction, along with Fermi-arc-like surface states in an array of laser-written waveguides [30] and hyperbolic [31] and helicoil [32] microwave metamaterials. Most recently a synthetic axial field was generated in a phononic Weyl model [33]. Such a spinful 3D model *must* exhibit nontrivial spin texture in the vicinity of a linear dispersion point (Weyl point), and this synthetic platform directly measures the Berry curvature associated with this spin texture.

By extending our Z_2 topological circuit [15,34] into the third dimension [35–37], we provide realization of Weyl particles in a circuit. In a 3D array of low-loss lumped circuit elements, we implement a cubic lattice with π flux per plaquette in all principal planes [38], realizing a Weyl band structure. Thanks to the exquisite control afforded by the circuit platform, we reveal the system's complex response with site-, energy- and spin-resolved microscopy. With the flexibility of nonlocal couplings between system edges, we impose periodic boundary conditions on some or all surfaces to probe both bulk and surface physics. We are thus able to measure the full spin-resolved band structure of the metamaterial. We extract the Berry curvature from the band structure and ascertain that the Weyl points are indeed quantized sources and sinks of Berry flux called "chiral charges." Finally, we perform a full reconstruction of the surface states vs momentum and energy and observe that the surface projections of the Weyl points are indeed connected by Fermi arcs.

I. ENGINEERING A WEYL CIRCUIT

The Weyl model that we realize in our circuit is analogous to a recent cold-atom proposal [38] that may be viewed as either a cubic lattice with π flux penetrating each plaquette in

*simonjon@uchicago.edu

 ©2019 American Physical Society

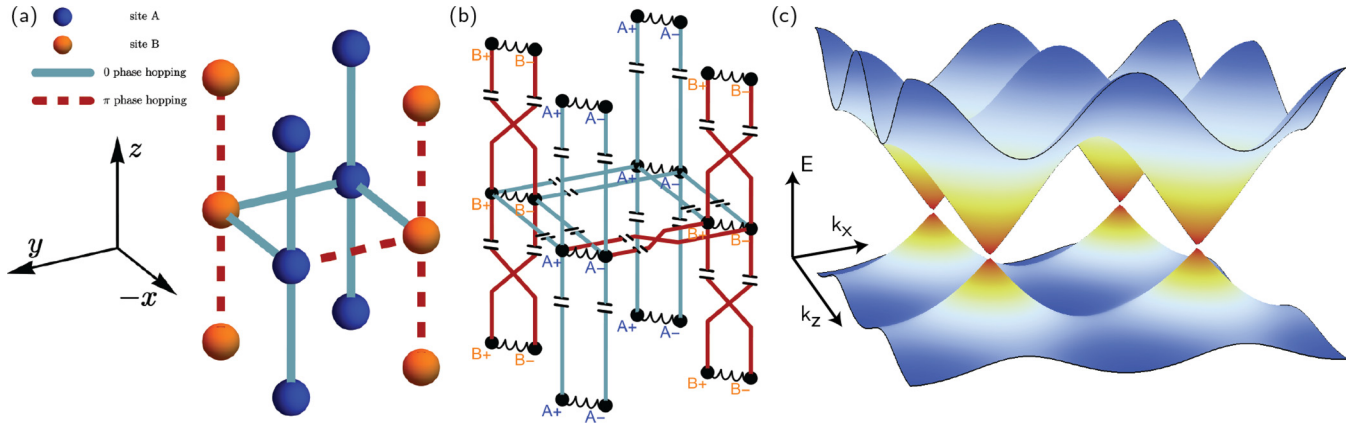

FIG. 1. A Weyl circuit. (a) Topology of the tunneling connectivity of a minimal lattice model exhibiting Weyl points. The unit cell consists of two sites, with A sites shown in blue and B sites shown in orange. Zero-phase tunneling is represented as a cyan solid line and π-phase tunneling as red dashed line. The lattice vectors are $\hat{z}$, $\hat{u} \equiv \frac{1}{\sqrt{2}}(\hat{x} + \hat{y})$, and $\hat{v} \equiv \frac{1}{\sqrt{2}}(\hat{x} - \hat{y})$. (b) To realize such a lattice with circuit components, all lattice sites are replaced by inductors, and all tunnel couplings by a pair of capacitors. A zero-phase tunnel coupling capacitively connects the positive end of one inductor to the positive end of its neighbor, and the negative end to the negative end of the neighbor. A π-phase tunnel connection capacitively couples the positive end of an inductor to the *negative* end of its neighbor, and vice versa. (c) Shows numerically calculated band structure at $k_y = 0$; apparent are four Weyl points in the first Brillouin zone.

each principal plane ($x - y$, $x - z$, and $y - z$), corresponding to a half-flux Hofstadter model in each plane (and a two-site magnetic unit cell), or equivalently a cubic lattice of spin-1/2's with engineered spin-dependent tunneling. In either case, it is a 3D time-reversal symmetric tight-binding model on a cubic lattice; the two sites in the *magnetic* unit cell generate the pseudospin degree of freedom in the spin model (see Fig. 1).

The dispersion relation of this tight-binding Hamiltonian is (see Supplemental Material for details [39]): $\mathcal{H}(\boldsymbol{k}) = \varepsilon_0 + \boldsymbol{h}(\boldsymbol{k}) \cdot \boldsymbol{\sigma}$, with $\boldsymbol{h}(\boldsymbol{k})/2t_0 = \cos(k_x a)\hat{x} - \sin(k_y a)\hat{y} + \cos(k_z a)\hat{z}$. The eigenenergies are thus: $E_{\pm}(\boldsymbol{k}) = \varepsilon_0 \pm 2t_0\sqrt{\cos^2(k_z a) + \cos^2(k_x a) + \sin^2(k_y a)}$. The four Weyl points are located at $\boldsymbol{k}a = \pi/2(\pm 1, 0, \pm 1)$, with energy $E = \varepsilon_0$ and chiral charges $\chi = -\mathrm{sgn}(k_x k_z)$.

The crucial technique required to realize this Weyl model in a circuit is the ability to generate a synthetic magnetic flux by controlling tunneling phase, which we achieve by capacitively coupling each end of each on-site inductor its neighbors; swapping the connections generates a π phase shift in the tunneling amplitude [15].

We assemble an $8 \times 8 \times 8$ lattice of two-site unit cells by stacking printed circuit boards (PCBs) with connectivity in x, y, and z directions shown in Fig. 1(b). The lattice translation vectors are $\hat{u} \equiv \frac{1}{\sqrt{2}}(\hat{x} + \hat{y})$, and $\hat{v} \equiv \frac{1}{\sqrt{2}}(\hat{x} - \hat{y})$, and $\hat{z}$, parallel to physical edges of the circuit boards. For the chosen component values (see Supplemental Material for details [39]), the predicted Weyl point frequency is $f_{\mathrm{Weyl}} =$ 290 kHz, and the band-structure spans the frequency range 230–450 kHz.

II. PROBING BULK TOPOLOGY

To probe the bulk band structure without surface-state contamination, we harness the unique control of our circuit realization [15] to impose periodic boundary conditions on all surfaces (see Supplemental Material for details [39]), thus realizing a finite system which is *all bulk*. We experimentally extract the band structure and spin texture of the Weyl circuit by measuring the frequency-dependent response of the circuit as a function of spatial offset using a custom-built 3D scanner (see Supplemental Material for details [39]). Because we recover the full magnitude and phase of the response, we are able to reconstruct (via a Fourier transform) the momentum-dependent response of the system. Plotting this response vs $\vec{k}$ yields the lattice-photon dispersion shown in Fig. 2(a), plotted in the vicinity of the Weyl point at $\boldsymbol{k} = (-\pi/2, 0, -\pi/2)$; at frequencies just above (or below) the Weyl frequency f_{Weyl} the equienergy surface is a near sphere around the Weyl point—as the frequency approaches f_{Weyl}, the response collapses to into the Weyl point. In Fig. 2(b), equienergy surfaces of the response are plotted over the full Brillouin zone for frequencies above f_{Weyl}, revealing four Weyl points whose momenta are, as anticipated, $\boldsymbol{k} = (\pm\pi/2, 0, \pm\pi/2)$.

Our ability to resolve the complex-valued response on both A and B sublattices permits a complete reconstruction of the spin texture of the Bloch states. The arrows in Fig. 2(b) reflect the measured spin structure of the momentum states on the upper energy surface; Figs. 2(c) and 2(d) are cuts at $k_z = \pi/2$ and $k_y = 0$, which are planes embedding two Weyl points, and all four, respectively. It is apparent that only near the Weyl point at $\boldsymbol{k} = (\pi/2, 0, \pi/2)$ does the spin points everywhere radially—an inward radial hedgehog defect, while the other three Weyl points exhibit hyperbolic hedgehogs; this is because we have chosen a uniform definition of the spin-Bloch sphere over the full Brillouin zone—each Weyl point may be converted into a radial hedgehog through a local spin transformation of even parity, from which the sign of the chiral charge of the corresponding Weyl point may be observed directly—outward/inward hedgehog for positive/negative chiral charge, respectively.

Note that topological considerations require Weyl points to come in pairs with opposite chiral charge [40]; when discrete

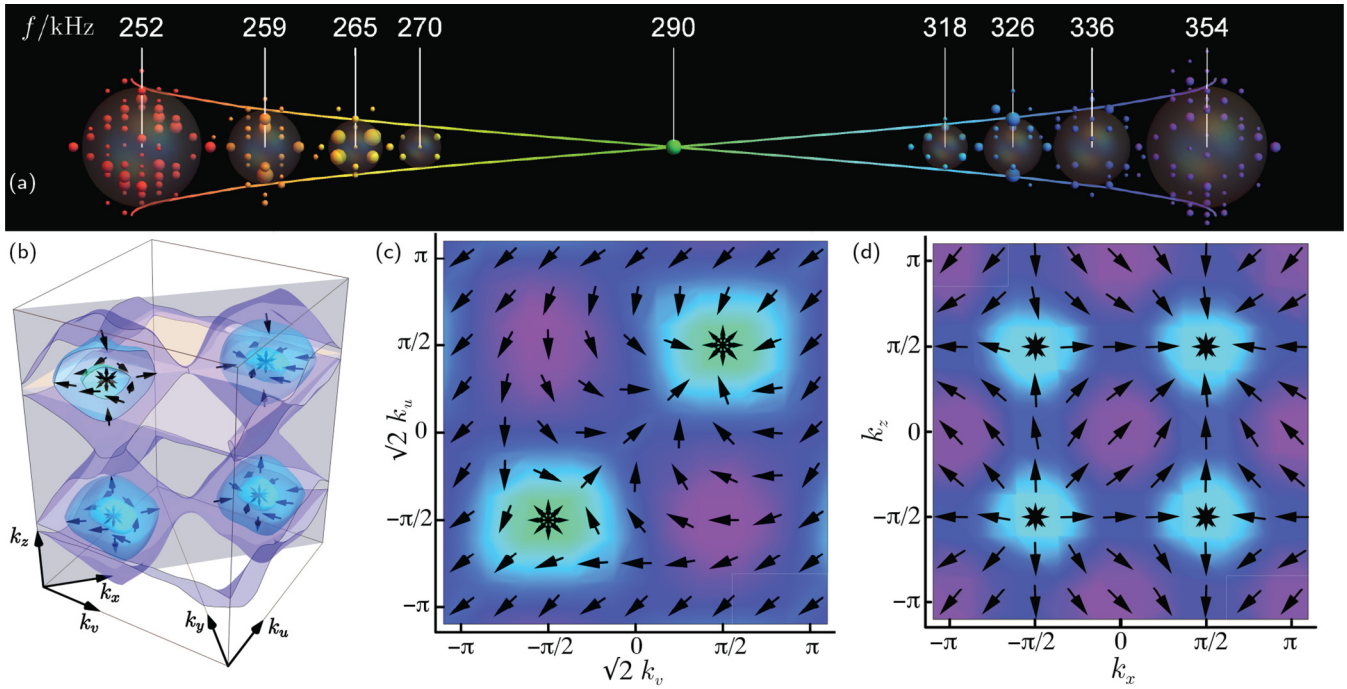

FIG. 2. Measured band structure of the Weyl circuit. In a configuration with periodic boundary conditions *physically imposed* along all three axes, it is possible to fully reconstruct the bulk band structure by exciting a single site and measuring the complex response at all sites as a function of frequency. A 3D spatial Fourier transform of the resulting response yields the dispersion shown in (a) in the vicinity of the Weyl point at $\boldsymbol{k} = (\pi/2, 0, \pi/2)$. The response below (red) and above (purple) the Weyl energy forms near-spherical shells in k space, made slightly square by the finite ($8 \times 8 \times 8$) system size. These shells form a conical (linear) dispersion around the Weyl point highlighted by the (red to purple) envelope surrounding the data. At the energy of the Weyl point (green), the response is localized *exclusively* to the momentum of the Weyl point. The equienergy surfaces are plotted over the full Brillouin zone in (b), for the band above the Weyl frequency [color scale same as (a)]. The equienergy surfaces are aspheric at frequencies far from the Weyl points, a generic result arising from the eventual merger of the Weyl cones into a single band. Also plotted (arrows) is the reconstructed spin texture of the upper band Bloch functions near the Weyl points; at $\boldsymbol{k} = (\pi/2, 0, \pi/2)$ the spin points everywhere inwardly—a radial hedgehog defect, while the other three Weyl points exhibit hyperbolic hedgehog defects, from which we can deduce the chirality of the Weyl points: $\chi = -\,\mathrm{sgn}(k_x k_z)$. In (c) we plot a slice of the measured dispersion in the $k_v - k_u$ plane at the $k_z = \pi/2$ of two Weyl points. In (d) we plot a slice in the $k_x - k_z$ plane at the $k_y = 0$ of all Weyl points. Also shown, as arrows, are the projections of all the spin texture into the planes.

translation is the sole remaining symmetry (inversion and time reversal are broken) the BZ may exhibit a single pair of Weyl points; the minimum is two pairs if time-reversal symmetry is preserved. The first Weyl fermions, observed in TaAs [41,42], did not break time-reversal symmetry and because of the complex structure of TaAs, exhibited 12 pairs of Weyl points. Our platform exhibits the minimum four pairs of Weyl points allowed for a time-reversal symmetric system.

From the measured space- and spin-resolved Bloch functions we are able to extract the Berry curvature pseudovector of the lower band $\boldsymbol{\Omega}(\boldsymbol{k})$ via (see Supplemental Material for details [39]): $\boldsymbol{\Omega}^{(n)}(\boldsymbol{k}) = i\langle \nabla_{\boldsymbol{k}}\psi_n(\boldsymbol{k})| \times |\nabla_{\boldsymbol{k}}\psi_n(\boldsymbol{k})\rangle$. The curvature is plotted in Fig. 3(a), and it is apparent that while the spin texture is gauge dependent, the Berry curvature is *not*—each Weyl point acts as either a source or sink of Berry curvature, evident from the flow of curvature into/out-of the points. The measured Berry curvature flow from sources to the sinks is shown in Fig. 3(b) and 3(c), where 2D slices of the full 3D Brillouin zone are displayed. The overlaid density plot depicts the measured chiral charge density $\rho_\chi \equiv \frac{1}{2\pi}\nabla_k \cdot \boldsymbol{\Omega}$, exhibiting two (maximally localized, delta-function-like) sources (positively charged, orange) and two sinks (negatively charged, blue), located at the four Weyl points. Integrating the Berry flux over a surface enclosing a single Weyl point yields chiral charges of $\chi = \frac{1}{2\pi}\oiint \boldsymbol{\Omega}\cdot\hat{\boldsymbol{n}}\,\mathrm{d}S = \iiint \rho_\chi \mathrm{d}V = +1, -1, +1, -1$, in agreement with theory (see Supplemental Material for details [39]).

III. PROBING SURFACE STATES

The chiral charge of the Weyl nodes is also reflected in the structure of the surface states. This is most easily understood [43] by considering a simple material with only one pair of Weyl nodes and examining the states on an infinite cylindrical surface whose axis $\hat{n}$ is aligned with the vector connecting the (oppositely charged) Weyl points. The resulting 2D band structure, when computed as a function of the axial momentum k_n, will exhibit chiral edge states when the Chern number at fixed k_n is nonzero (see Supplemental Material for details [39]). The momentum structure of these surface states is model dependent, but the surface channel must terminate at the projections of the Weyl points onto the surface, yielding "Fermi arcs" at f_{Weyl} connecting the Weyl points; additional Weyl points (as in our experiment) result in more arcs. More broadly, Fermi arcs only present on particular surfaces (see Supplemental Material for details [39]).

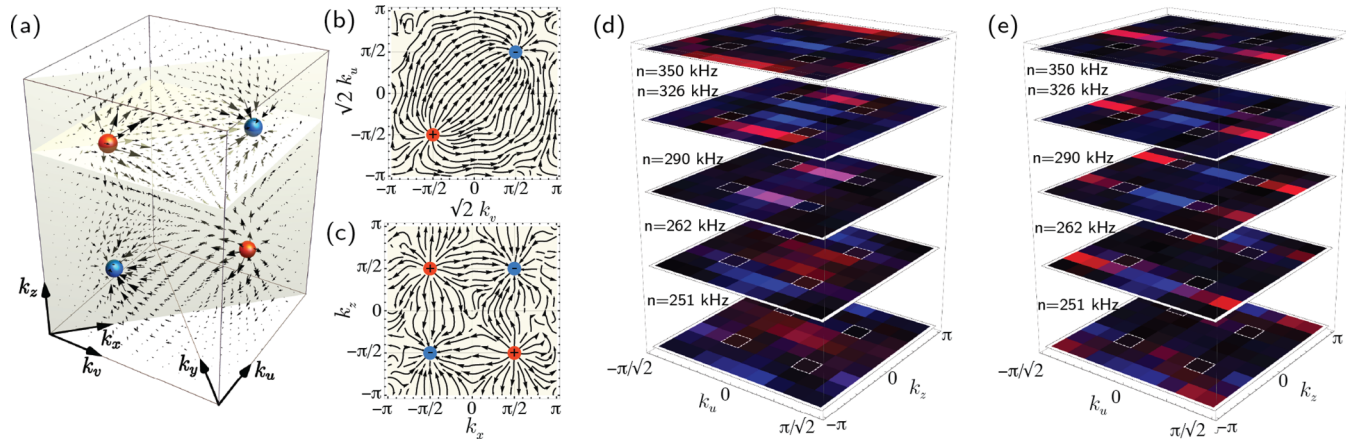

FIG. 3. Measured Berry curvature, Berry flux, and surface states. (a) shows the measured and interpolated Berry curvature (arrows), and associated Berry flux (blue→ orange is negative → positive), over the full Brillouin zone, for the lower band. Divergence of the Berry curvature is strictly zero except at four topological defects located at the Weyl points, carrying ±1 chiral charge, with +1 corresponding to sources of Berry flux (orange), and −1 to sinks (blue), evident from the flow of the Berry curvature. Slices along $k_v - k_u$ and $k_x - k_z$ are shown in (b) and (c), respectively, highlighting the structure of this flow. (d) and (e) show the measured surface states for even and odd numbers of layers in the v direction, respectively. States residing on the top surface are depicted in shades of red proportional to excitation amplitude, while those on the bottom surface are depicted in shades of blue. Only selected frequency planes are shown here and within each plane is a 8×8 pixels surface Brillouin zone, limited by the system size as also shown in the Supplemental Material. It is apparent that, in the $\nu = f_{\text{Weyl}} = 290$ kHz plane, the surface projection of the Weyl points (outlined in dashed white squares) are connected by lines ("Fermi arcs") of surface states; for an even number of layers, the Fermi arcs are within the Brillouin zone and overlap each other on both top and bottom surfaces, while for an odd number of layers the Fermi arc on the top surface (red) passes *around* the Brillouin zone, exploiting its toroidal topology—a consequence of the gauge difference between even and odd layers (see Supplemental Material for details [39]).

We experimentally probe the surface physics by removing the periodic boundaries on the $\hat{v}$ axis (see Supplemental Material for details [39]) and repeating our site-resolved measurements on the faces of the resulting three cylinder. The measured surface band structure is shown in Figs. 3(d) and 3(e); the Fermi arcs manifest as lines in $k_u - k_z$ space, linking the surface projections of the pairs of Weyl points at a frequency of 290 kHz. When the metamaterial has an even number of layers, the arcs on the top and bottom surfaces follow the same path through the BZ. When the metamaterial has an odd number of layers, the Fermi arcs on the top surface connect the Weyl points through the BZ, and around the edge of the (toroidal) BZ on the bottom surface, as anticipated theoretically [44].

In conclusion, we have realized the first circuit supporting Weyl particles as excitations and explored its properties: We find two pairs of Weyl points, and by spin-resolved spectroscopy directly map out the Berry curvature over the full Brillouin zone, thereby ascertaining that the Weyl points in each pair have opposite quantized chiral charge. Further evidence of the chiral charge of the Weyl points comes from the direct detection of Fermi-arc surface states connecting their surface projections. The addition of ferrites will enable realization of even more robust T-broken models [16], while application of quantum circuit techniques [45] will enable qubit-mediated interactions [22], enabling study of the interplay of topology and many-body physics [46–49].

IV. METHODS

The lattice is composed of eight stacked printed circuit boards (PCBs), each containing two interleaved 8×8 sublattices of inductors, capacitively coupled on both ends to their nearest neighbors (see Supplemental Material for details [39]). The eight boards are further capacitively coupled together through additional interboard headers. Periodic boundary conditions are imposed by connecting the opposite faces of the bulk together using ribbon cables (see Supplemental Material for details [39]).

Each unit cell is composed of $2 \times 1.02(1)$ mH inductors and $12 \times 100(2)$ pF capacitors. A single inductor-capacitor pair has a measured Q factor of 136(9) [in the frequency range from 233(3) kHz to 409(3) kHz], limited by inductor ohmic loss. We probe the lattice using an RF network analyzer to excite a single lattice site (inductor) via a magnetically-coupled drive coil and measure site-by-site using a magnetic pick-up coil that is translated from site-to-site in the lattice using a heavily modified 3D printer.

The circuit platform offers unique benefits including: *the ability to perform site-resolved measurements of (complex) transport coefficients*—a probe coil may be placed inside the bulk to excite and measure the amplitude and phase response at any site; *exquisite control of global topology*—in each dimension one may choose between periodic boundaries and (sharp) open boundaries, the former proposed but unrealized in optical lattices [50], and the latter only recently achieved using real [51–53] or synthetic [54–56] dimensions; more exotic topologies [57] such as Mobiüs strips [15] and Klein bottles are also possible, along with non-Euclidean geometries arising from modified connectivity [58].

Note added. We recently became aware of the work of Helbig *et al.*, providing a new formalism, the "impedance band structure," of circuit arrays [59].

ACKNOWLEDGMENTS

The authors would like to thank Michael Levin for fruitful discussions. This work was supported by DOE Grant No. DE-SC0010267 for apparatus construction/data collection and MURI Grant No. FA9550-16-1-0323 for analysis. D.I.S. acknowledges support from the David and Lucile Packard Foundation. This work was also supported by the University of Chicago Materials Research Science and Engineering Center, which is funded by National Science Foundation under Award No. DMR-1420709.

[1] I. Bloch, J. Dalibard, and W. Zwerger, Rev. Mod. Phys. **80**, 885 (2008).

[2] I. Carusotto and C. Ciuti, Rev. Mod. Phys. **85**, 299 (2013).

[3] N. Goldman, G. Juzeliūnas, P. Öhberg, and I. B. Spielman, Rep. Prog. Phys. **77**, 126401 (2014).

[4] M. Hafezi, E. A. Demler, M. D. Lukin, and J. M. Taylor, Nat. Phys. **7**, 907 (2011).

[5] A. C. Mahoney, J. I. Colless, S. J. Pauka, J. M. Hornibrook, J. D. Watson, G. C. Gardner, M. J. Manfra, A. C. Doherty, and D. J. Reilly, Phys. Rev. X **7**, 011007 (2017).

[6] L. Tarruell, D. Greif, T. Uehlinger, G. Jotzu, and T. Esslinger, Nature (London) **483**, 302 (2012).

[7] K. K. Gomes, W. Mar, W. Ko, F. Guinea, and H. C. Manoharan, Nature (London) **483**, 306 (2012).

[8] G. Jotzu, M. Messer, R. Desbuquois, M. Lebrat, T. Uehlinger, D. Greif, and T. Esslinger, Nature (London) **515**, 237 (2014).

[9] Y.-J. Lin, K. Jiménez-García, and I. B. Spielman, Nature (London) **471**, 83 (2011).

[10] B.-Z. Wang, Y.-H. Lu, W. Sun, S. Chen, Y. Deng, and X.-J. Liu, Phys. Rev. A **97**, 011605 (2018).

[11] Y.-J. Lin, R. L. Compton, K. Jimenez-Garcia, J. V. Porto, and I. B. Spielman, Nature (London) **462**, 628 (2009).

[12] M. Hafezi, S. Mittal, J. Fan, A. Migdall, and J. Taylor, Nat. Photonics **7**, 1001 (2013).

[13] Z. Wang, Y. Chong, J. D. Joannopoulos, and M. Soljačić, Nature (London) **461**, 772 (2009).

[14] M. C. Rechtsman, J. M. Zeuner, Y. Plotnik, Y. Lumer, D. Podolsky, F. Dreisow, S. Nolte, M. Segev, and A. Szameit, Nature (London) **496**, 196 (2013).

[15] J. Ningyuan, C. Owens, A. Sommer, D. Schuster, and J. Simon, Phys. Rev. X **5**, 021031 (2015).

[16] C. Owens, A. LaChapelle, B. Saxberg, B. M. Anderson, R. Ma, J. Simon, and D. I. Schuster, Phys. Rev. A **97**, 013818 (2018).

[17] N. Schine, A. Ryou, A. Gromov, A. Sommer, and J. Simon, Nature (London) **534**, 671 (2016).

[18] R. Süsstrunk and S. D. Huber, Science **349**, 47 (2015).

[19] L. M. Nash, D. Kleckner, A. Read, V. Vitelli, A. M. Turner, and W. T. Irvine, Proc. Natl. Acad. Sci. **112**, 14495 (2015).

[20] M. E. Tai, A. Lukin, M. Rispoli, R. Schittko, T. Menke, D. Borgnia, P. M. Preiss, F. Grusdt, A. M. Kaufman, and M. Greiner, Nature (London) **546**, 519 (2017).

[21] M. Lewenstein, A. Sanpera, V. Ahufinger, B. Damski, A. Sen, and U. Sen, Adv. Phys. **56**, 243 (2007).

[22] A. Wallraff, D. I. Schuster, A. Blais, L. Frunzio, R.-S. Huang, J. Majer, S. Kumar, S. M. Girvin, and R. J. Schoelkopf, Nature (London) **431**, 162 (2004).

[23] T. Peyronel, O. Firstenberg, Q.-Y. Liang, S. Hofferberth, A. V. Gorshkov, T. Pohl, M. D. Lukin, and V. Vuletić, Nature (London) **488**, 57 (2012).

[24] N. Jia, N. Schine, A. Georgakopoulos, A. Ryou, L. W. Clark, A. Sommer, and J. Simon, Nature Phys. **14**, 550 (2018).

[25] N. P. Armitage, E. J. Mele, and A. Vishwanath, Rev. Mod. Phys. **90**, 015001 (2018).

[26] L. Lu, Z. Wang, D. Ye, L. Ran, L. Fu, J. D. Joannopoulos, and M. Soljačić, Science **349**, 622 (2015).

[27] W.-J. Chen, M. Xiao, and C. T. Chan, Nat. Commun. **7**, 13038 (2016).

[28] A. A. Soluyanov, D. Gresch, Z. Wang, Q. Wu, M. Troyer, X. Dai, and B. A. Bernevig, Nature (London) **527**, 495 (2015).

[29] Y. Xu, F. Zhang, and C. Zhang, Phys. Rev. Lett. **115**, 265304 (2015).

[30] J. Noh, S. Huang, D. Leykam, Y. Chong, K. P. Chen, and M. C. Rechtsman, Nat. Phys. **13**, 611 (2017).

[31] B. Yang, Q. Guo, B. Tremain, L. E. Barr, W. Gao, H. Liu, B. Béri, Y. Xiang, D. Fan, A. P. Hibbins *et al.*, Nat. Commun. **8**, 97 (2017).

[32] B. Yang, Q. Guo, B. Tremain, R. Liu, L. E. Barr, Q. Yan, W. Gao, H. Liu, Y. Xiang, J. Chen *et al.*, Science **359**, 1013 (2018).

[33] V. Peri, M. Serra-Garcia, R. Ilan, and S. D. Huber, arXiv:1806.09628.

[34] V. V. Albert, L. I. Glazman, and L. Jiang, Phys. Rev. Lett. **114**, 173902 (2015).

[35] C. H. Lee, S. Imhof, C. Berger, F. Bayer, J. Brehm, L. W. Molenkamp, T. Kiessling, and R. Thomale, Commun. Phys. **1**, 39 (2018).

[36] K. Luo, R. Yu, and H. Weng, Research **2018**, 6793752 (2018).

[37] Y. Yang, Z. Gao, H. Xue, L. Zhang, M. He, Z. Yang, R. Singh, Y. Chong, B. Zhang, and H. Chen, arXiv:1804.03595.

[38] T. Dubček, C. J. Kennedy, L. Lu, W. Ketterle, M. Soljačić, and H. Buljan, Phys. Rev. Lett. **114**, 225301 (2015).

[39] See Supplemental Material at http://link.aps.org/supplemental/10.1103/PhysRevB.99.020302 for details on modeling, apparatus construction, data collection, and data analysis.

[40] H. B. Nielsen and M. Ninomiya, Phys. Lett. B **105**, 219 (1981).

[41] B. Lv, H. Weng, B. Fu, X. Wang, H. Miao, J. Ma, P. Richard, X. Huang, L. Zhao, G. Chen *et al.*, Phys. Rev. X **5**, 031013 (2015).

[42] S.-Y. Xu, I. Belopolski, N. Alidoust, M. Neupane, G. Bian, C. Zhang, R. Sankar, G. Chang, Z. Yuan, C.-C. Lee *et al.*, Science **349**, 613 (2015).

[43] M. Z. Hasan, S.-Y. Xu, I. Belopolski, and S.-M. Huang, Annu. Rev. Condens. Matter Phys. **8**, 289 (2017).

[44] P. Hosur, Phys. Rev. B **86**, 195102 (2012).

[45] B. M. Anderson, R. Ma, C. Owens, D. I. Schuster, and J. Simon, Phys. Rev. X **6**, 041043 (2016).

[46] B. Roy, P. Goswami, and V. Juričić, Phys. Rev. B **95**, 201102 (2017).

[47] C. Chan and X.-J. Liu, Phys. Rev. Lett. **118**, 207002 (2017).

[48] P. Buividovich and M. Puhr, PoS **(LATTICE2014)** 061 (2014).

[49] H. Wei, S.-P. Chao, and V. Aji, Phys. Rev. Lett. **109**, 196403 (2012).
[50] M. Łącki, H. Pichler, A. Sterdyniak, A. Lyras, V. E. Lembessis, O. Al-Dossary, J. C. Budich, and P. Zoller, Phys. Rev. A **93**, 013604 (2016).
[51] A. L. Gaunt and Z. Hadzibabic, Sci. Rep. **2**, 721 (2012).
[52] P. M. Preiss, R. Ma, M. E. Tai, A. Lukin, M. Rispoli, P. Zupancic, Y. Lahini, R. Islam, and M. Greiner, Science **347**, 1229 (2015).
[53] B. Mukherjee, Z. Yan, P. B. Patel, Z. Hadzibabic, T. Yefsah, J. Struck, and M. W. Zwierlein, Phys. Rev. Lett. **118**, 123401 (2017).
[54] B. Stuhl, H.-I. Lu, L. Aycock, D. Genkina, and I. Spielman, Science **349**, 1514 (2015).
[55] M. Mancini, G. Pagano, G. Cappellini, L. Livi, M. Rider, J. Catani, C. Sias, P. Zoller, M. Inguscio, M. Dalmonte *et al.*, Science **349**, 1510 (2015).
[56] A. Celi, P. Massignan, J. Ruseckas, N. Goldman, I. B. Spielman, G. Juzeliūnas, and M. Lewenstein, Phys. Rev. Lett. **112**, 043001 (2014).
[57] A. Weststrom and T. Ojanen, Phys. Rev. X **7**, 041026 (2017).
[58] R. R. Biswas and D. T. Son, Proc. Natl. Acad. Sci. **113**, 8636 (2016).
[59] T. Helbig, T. Hofmann, C. H. Lee, R. Thomale, S. Imhof, L. W. Molenkamp, and T. Kiessling, arXiv:1807.09555.